Readapting PhaseNet to Laboratory Earthquakes: AEsNet, a Robust Acoustic Emission Picker Illuminating Seismic Signatures of Different Fault Gouge Materials

Mastella G.[1], Poggiali G.[1], Pignalberi F.[1], and Scuderi M.[1]

[1]Sapienza University of Rome, Earth Sciences, Italy.

Corresponding author: Giacomo Mastella (giacomo.mastella@uniroma1.it)
Author ORCIDs:

- Giacomo Mastella: `https://orcid.org/0000-0002-9052-4873`
- Giulio Poggiali:
- Federico Pignalberi: `https://orcid.org/0000-0002-4153-37.9X`
- Marco Scuderi: `https://orcid.org/0000-0001-5232-0792`

Abstract

Laboratory acoustic emissions (AEs) represent microslip events analogous to small-scale earthquakes, providing valuable insights into the mechanics of frictional instabilities. With technological advancements in acoustic monitoring, thousands of AE waveforms can now be collected in minutes of experimental time, requiring efficient methods for their detection and analysis. In this study, we introduce a deep learning model for automatically detecting AEs in laboratory shear experiments. Our dataset consists of about 30,000 manually picked AEs waveforms collected under different experimental boundary conditions using two fault gouge materials: Min-U-Sil quartz gouge and glass beads. By adapting the PhaseNet model, originally developed for natural earthquake phase detection, we train AEsNet, a robust AE picker that outperforms pre-existing picking methods for the tested materials. To investigate whether the trained models can generalize across different boundary conditions and materials, and overcome the limitations of small, manually labeled datasets, we apply transfer learning to analyze performance relative to training size and material diversity. Our results indicate that model performance is largely independent of experimental conditions but strongly dependent on material type. This finding suggests that direct transfer of models trained on one material to another is often ineffective due to distinct frequency characteristics of AEs, which are closely linked to the microphysical processes driving emissions in the different granular materials. However, quick fine-tuning significantly enhances pre-trained AEsNet performance, even surpassing that of a fine-tuned PhaseNet model pre-trained on natural earthquakes. This underscores the importance of customizing models to the specific attributes of laboratory-generated AEs—a conclusion consistent with findings from transfer learning applications in natural seismicity. In conclusion, our approach provides an efficient tool for enhancing AE detection, even with limited data from diverse laboratory conditions, enabling the creation of reliable AE catalogs that can significantly advance our understanding of fault mechanics in controlled experimental settings.

1 Introduction

Acoustic emissions (AEs) represent elastic waves generated by the release of energy from micromechanical processes (fractures or frictional sliding) within a material under deformation. Given their small source, AEs emit high-frequency seismic signals ranging from tens of kHz to MHz Lei and Ma (2014), requiring the use of high central frequency transducers such as piezoelectric transducers (PZTs) to capture them effectively. Since the 1960s, AEs observed during rock deformation experiments have been recognized as microslip events analogous to natural earthquakes, and have been used to study seismogenic processes in controlled laboratory settings Mogi (1962), Scholz (1968), Lockner et al. (1991), Johnson et al. (2013). Large AE catalogs have demonstrated that these events follow statistical distributions similar to those of natural earthquakes, including power-law size-frequency distributions Gutenberg and Richter (1944), Mogi (1962), Scholz (1968), and aftershock sequences governed by Omori's law Omori (1894), Mogi (1966). Analyzing the rate and amplitude of AEs throughout the seismic cycle can yield valuable insights into fault dynamics. These microslip events, which often precede the main failure, exhibit non-random patterns that provide critical information about the nucleation process leading to dynamic rupture. Statistical analyses of AE parameters, such as the b-value Main et al. (1989), Main (1992), Dresen et al. (2020), Goebel et al. (2017), Kwiatek et al. (2014), Shreedharan et al. (2019), McLaskey and Kilgore (2013), Rivière et al. (2018), Bolton et al. (2021), Korkolis et al. (2021), along with the spatiotemporal evolution of AE waveforms Bolton et al. (2023), Kwiatek et al. (2024), suggest that the increase of these events and their tendency to cluster both spatially and temporally, might signal the initiation of an instability Marty et al. (2023), Goebel et al. (2024). During this phase, micro-scale frictional asperities fail, potentially coalescing and ultimately triggering larger failures. These asperity-scale processes Shreedharan et al. (2020) often lead to an exponential increase in acoustic power before failure, a characteristic that enables machine learning models to predict laboratory earthquakes Rouet-Leduc et al. (2017, 2018), Lubbers et al. (2018), Hulbert et al. (2019), Karimpouli et al. (2023), Wang et al. (2022). AEs can thus be viewed as stress meters Goebel et al. (2013), Bolton et al. (2020), providing real-time insight into stress evolution. Moreover, removing the influence of the monitoring system (commonly referred to as the instrument apparatus response) from the AE signals, allows for source characterization through seismological spectral analysis McLaskey and Glaser (2012), McLaskey et al. (2015), Pignalberi et al. (2024), providing valuable information on source properties and energy partitioning during dynamic rupture events. This analysis is essential for scaling observations from laboratory experiments to natural earthquakes Goodfellow and Young (2014), Selvadurai (2019), Blanke et al. (2021).

Recent advancements in acoustic monitoring systems, now capable of operating at MHz sampling rates, enable the collection of thousands of AEs within minutes of experimental time Rivière et al. (2018), highlighting the critical need for fast and reliable detection and analysis methods. However, in laboratory experiments, several factors complicate their detection. A major challenge is experimental noise, often generated by hydraulic power supplies or electrical motors in laboratory earthquake machines. Furthermore, AEs frequently occur in large numbers and close succession, leading to overlapping waveforms that, along with scattering, can obscure clear first AE arrivals. AE detection accuracy is also heavily influenced by PZT characteristics, particularly their inherent polarization which leads to preferential sensitivity to either P- or S-waves. The angle of wave incidence relative to the sensor orientation can substantially affect arrival clarity, resulting in varying detection capabilities across different source locations. Additionally, while PZTs operate across a broad frequency spectrum, they typically work in resonance and lack a flat response, which can significantly influence the recorded AE waveforms making first-arrival picking even more challenging.

Standard amplitude based picking methods include the short-term average/long-term average (STA/LTA) method Allen (1978), which detects seismic arrivals by tracking the ratio of seismic energy in two time windows. The STA window (ST) focuses on capturing sudden increases in signal amplitude, while the long-term window (LT) establishes the baseline noise level. When the STA/LTA ratio surpasses a predefined threshold, it indicates the arrival of a P or S wave. Another common technique involves joint autoregressive (AR) modeling of noise and seismic signals, using the Akaike Information Criterion (AIC) to identify seismic signal onset Sleeman and Van Eck (1999). While generally efficient, these methods are susceptible to noise and may lack accuracy when precise arrival times are required. They are particularly challenging to apply when target waveforms are closely spaced in time, a common occurrence with AEs during laboratory experiments on granular materials Johnson et al. (2013), Bolton et al. (2020). Additionally, all of these methods require the tuning of numerous empirical hyperparameters, which are dependent on factors such as monitoring rate, sensor types, waveform characteristics, experimental noise, and, most importantly, user input trial-and-error adjustments. This makes the picking procedure tedious and highly user-dependent, as optimal parameter settings must be tailored to each specific experimental condition.

Recently, deep learning (DL) have shown promise in overcoming some of these challenges in the context of natural earthquakes. In earthquake seismology, DL methods have become standard for phase picking Zhu and Beroza (2019), Perol et al. (2018), Ross et al. (2018), Soto and Schurr (2021), Mousavi et al. (2020), significantly enhancing the detection of smaller events and thereby improving the completeness and resolution of earthquake catalogs (e.g., Tan et al. (2021)). Trugman et al. Trugman et al. (2020) were the first to apply DL for detecting AE in laboratory shear experiments, despite working with a model trained on natural earthquakes and a limited catalog not manually labeled. Recently, Shi et al. Shi et al. (2024) proposed a workflow to enhance the performance of pre-trained seismic picking models on out-of-distribution datasets without requiring retraining, by applying data rescaling, filtering, and prediction ensembling. The method, which employs DL models trained on natural earthquakes, has been tested on various seismic datasets across different spatial and temporal scales, as well as on AEs recorded during a triaxial rock deformation experiment on Berea sandstone.

Despite these advancements, there remains a lack of well-established ML models specifically for AE detection in laboratory settings, likely due to the scarcity of large, manually annotated AE catalogs. To address this gap, we leverage an extensive dataset of manually revised AE picks from shear experiments conducted under various boundary conditions, using different types of PZTs sensors and with different gouge materials, glass beads and quartz granular gouge. We train an adapted version of the PhaseNet model Zhu and Beroza (2019) originally developed for earthquake phase detection, to enable automatic AEs detection. We demonstrate that our model, which we call AEsNet, outperforms pre-existing picking techniques. To address the challenge of limited training datasets, we propose a transfer learning approach. We evaluate the prediction performance and limitations of our models in relation to the underlying physical behaviors of the different granular materials generating AEs. AEsNet results in a robust and adaptable tool that enhances AE detection and analysis in experimental seismology, improving efficiency and accuracy in processing large event catalogs.

2 Data and Methods

In this study, we rely on AEs detected during laboratory experiments run with the biaxial apparatus, BRAVA2, housed in the Rock Mechanics and Earthquake Physics Laboratory at Sapienza University of Rome (Figure 1A). The biaxial apparatus consists of two orthogonal servo-controlled hydraulic pistons used to apply normal and shear load on the samples. Each piston is equipped with a strain gauge load cell to measure the applied forces with a precision of ±0.03MPa. Displacement transducers (Linear Variable Differential Transformers, LVDTs) are fixed between the load frame and the moving piston to measure piston movement with sub-micron resolution, less than 0.1μm/s.

Experiments were performed in a double direct-shear configuration, where two 3-mm thick gouge layers are sandwiched between three steel forcing blocks characterized by two stationary side blocks (friction area 50 × 50 mm^2) and a central forcing block (80 × 50 mm^2, see inset in Figure 1A). The forcing blocks have grooves perpendicular to the shear direction (0.8 mm high and 2 mm spacing) to ensure shear localization within the gouge layers and not at the boundary with the steel blocks. The vertical ram moves at a constant displacement rate, applying shear stress and inducing shear deformation within the sample. On the central block, an on-board LVDT is mounted to directly measure fault displacement. All mechanical signals (stress and displacement) are recorded and digitized in real-time at 10 kHz using a multi-channel analog-to-digital converter (NI-9403) with 24-bit resolution. Four acoustic sensors (PZTs from Physik Instrument Ceramic, made from modified lead zirconate–lead titanate, PIC 255), are mounted on each of the forcing blocks to capture high-frequency AEs, resulting in a total of eight sensors in the double direct shear configuration. The PZT array on each block consists of two axial disk polarized parallel to the sensor surface, specifically more sensitive to compressional P waves, and two shear plates polarized perpendicular to the sensor surface, with one rotated 90° relative to the other to enhance sensitivity to shear Sv waves (moving vertically in the imposed shear direction) and shear Sh waves (moving along the block plane but perpendicular to the vertical direction) (Figure 1B). Accordingly, we refer to them as P, Sv and Sh sensors. This configuration simulates a three-component seismic station on each side block.

We performed experiments using two different types of fault gouges: fine grained quartz (Min-U-Sil 40 U.S. Silica Company) and glass beads (class IV spheres, grain size 150 µm). We chose these two gouges since they have been widely used in past laboratory experiments(e.g., Leeman et al. (2016), Johnson et al. (2013)) as discussed in the next section. Figure 1C shows a typical experiment. The gouge material is sheared at a constant sliding velocity of 10 µm/s. After a first elastic loading phase, during which the shear stress builds up, two unload-reload cycles are performed to promote shear localization and the formation of a steady-state shear fabric (Figure 1C). With accumulated deformation we observe the spontaneous emergence of unstable stick-slip behavior, typical of this material whose stress drop and recurrence time is controlled by the applied normal stress (e.g., Leeman et al. (2016)). As the stick-slip instabilities begin, experiments are acoustically monitored using the eight PZTs mounted on the two lateral blocks. The PZT analog signals are digitized by four two-channel TiePie Handyscope HS5 digital oscilloscopes with 16-bit resolution and a sampling rate of 3.125 MHz or 6.25 MHz (Figure 1B).

TiePie oscilloscopes also record the shear force applied to the sample for accurate synchronization with the mechanical data. Signal alignment is performed by downsampling the shear stress recorded by the oscilloscopes and cross-correlating its derivative with the derivative of the stress measured by the mechanical recording system. An example of 7 seconds of raw acoustic data and shear stress collected with the oscilloscope is reported in Figure 2A and Figure 2D, respectively for quartz and glass beads. Further details of the monitoring system and experimental procedure are provided in Pignalberi et al. (2024).

2.1 Dataset

Our dataset comprises AEs collected from double direct shear experiments using Min-U-Sil quartz powder and glass beads to simulate fault gouge. Min-U-Sil has been extensively studied to reproduce the full spectrum of slip behaviors from slow to fast stick-slip and explore the role of strain localization in controlling fault stability (e.g., Leeman et al. (2016), Scuderi et al. (2017), Bedford and Faulkner (2021)). Furthermore, it has been acoustically monitored to investigate laboratory earthquake nucleation processes (e.g., Bolton et al. (2020)). Similarly, glass beads have been extensively employed to explore the microphysics of frictional instabilities. The physics of this material is governed by force chain interactions (Mair et al. (2002), Scuderi et al. (2014)), which are encoded in AEs activity and control stress accumulation and release during fault stick-slip motion (e.g.,Johnson et al. (2013), Rivière et al. (2018)). Our dataset of AEs generated in Min-U-Sil consists of 22,000 manually picked AE waveforms, generated from different experiments, performed under a range of applied normal loads (from 6 MPa to 50 MPa). For glass beads, the dataset consists of 3,200 waveforms, all collected at a normal load of 6 MPa to avoid grain breakege during deformation Mair et al. (2002). AE waveform first arrivals have been manually picked by seven different operators using Snuffler, a seismogram browser that allows fast visualization and picking of seismic waveforms Heimann et al. (2017). Our analysis focuses only on P-wave first arrivals, excluding S waves, as the short 1.5 cm distance between the possible AE source and PZT sensors in our setup hinders their clear separation.

Each manually picked waveform in our dataset is classified based on the gouge material, applied normal stress, and, since the same AE event is recorded using different PZTs, also by sensor type and orientation, as illustrated in Figures 2C and 2F. The number of picks for P sensors is smaller than for Sv and Sh, as P sensors are more sensitive to hydraulic noise from the horizontal servo-hydraulic piston.

2.2 Model setup

As in the original PhaseNet model, manually picked arrivals are converted into probabilities, assigning the highest probability to the time point identified by the analysts, with nearby points receiving progressively lower probabilities based on a Gaussian distribution. This probabilistic representation of manual picks helps the algorithm mitigate the impact of picking errors within the dataset. We set the standard deviation of the Gaussian to 40 samples (6.4 or 12.8 microseconds at 6.25 MHz or 3.125 of sampling rate), reflecting the maximum time difference of AE first arrivals recorded between the most distant sensors for the tested materials in our experimental configuration. The probabilities represent the model's target, while the inputs are the unprocessed AE waveforms. We intentionally avoid band-pass filtering the waveforms to make our picker model more robust against hydraulic and electrical noise from the apparatus and monitoring system. These noises arises from the feedback control hydraulic system applying the normal load and power line interference affecting the PZT sensors.

The input waveforms and output probability sequences contain 9000 data points, in contrast to the 3000 points of the original PhaseNet version for natural earthquakes. A longer window offers two advantages: 1) it helps the model handle examples with multiple target picks by increasing the likelihood of having multiple events in the same waveform, and 2) it provides better sampling of the noise before and after AEs. The positions of the arrivals within the window are varied to ensure that the algorithm does not simply learn the windowing scheme. Each training example in our setup comprises a three-component array: one trace is a single waveform recorded with a single-component PZT, while the other two are zeroed. Each channel corresponds to a specific sensor type (P, SH, or SV), enabling the model to independently learn waveform features associated with each sensor type. This is fundamental because each sensor type has a different response that may alter waveform characteristics and is more sensitive to either P or S waves due to the piezoelectric polarization Pignalberi et al. (2024). Each waveform is normalized by removing its mean and dividing it by its standard deviation. To enhance the model's generalization capability during training, we randomly stacked event waveforms by shifting, scaling, and flipping their polarity. Overlapping event regions were avoided through the application of masks on phase, event, and polarity features, along with careful shifting to maintain distinct event boundaries.

An example of training waveforms for the same AE recorded by different PZT sensors for the different tested materials is shown in Figures 2B and 2E. We divided both the glass beads and Min-U-Sil datasets into training (60%), validation (10%), and testing (30%) subsets. The training and validation sets were used for model training and hyperparameters tuning, respectively, while the testing set was reserved for evaluating the final performance of AEsNet. For the testing set of AE waveforms, we added an equal number of noise waveforms collected during our experiments, enabling the model performance evaluation on both signals and noise. The data split was conducted independently of waveform characteristics. Separate models were trained for the glass beads and Min-U-Sil quartz gouge datasets.

2.3 Deep Learning Method

In this work, we use an adapted version of the original PhaseNet model Zhu and Beroza (2019), which is based on the U-Net convolutional autoencoder architecture Ronneberger et al. (2015) for processing 1-D time-series data. We use the PhaseNet implementation included in the EQNet package Zhu et al. (2022). Our AEsNet model takes AE waveforms as input and outputs binary probability distributions for P waves and noise, ranging from 0 (noise) to 1 (AE). The loss function is defined using cross-entropy between the true probability distribution ($p(x)$) and predicted distribution ($q(x)$).

While the autoencoder architecture remains identical to that of PhaseNet, we slightly modified the standard softmax normalization exponential function used to set probabilities in the final layer, ensuring greater numerical stability. Specifically, we subtract the maximum value along the relevant input tensor dimension before applying the exponential operation. This adjustment helps prevent issues related to floating-point precision, such as excessively large exponentials that can cause overflow or underflow.

The P arrival times are identified by extracting the picks of the output probability distributions after applying a threshold. For more detailed and technical specifications, we refer to the original PhaseNet paper Zhu and Beroza (2019).

3 Results

3.1 AEsNET performance evaluation

We evaluate the performance of our trained models following a binary classification framework. The models produce "positive" or "negative" outcomes based on the accuracy of the predicted result, identifying either noise or a pick. Four scenarios are possible: true positive (TP), true negative (TN), false positive (FP), and false negative (FN). We calculate precision, recall, and F1 score for each trained model.

Precision is:

$$P = \frac{TP}{TP + FP},$$

representing the proportion of positive identifications that were actually correct. Recall measures the ability to identify all relevant instances:

$$R = \frac{TP}{TP + FN},$$

and the F1 score combines both precision and recall to provide a balanced evaluation:

$$F1 = 2 \cdot \frac{P \cdot R}{P + R}.$$

Considering true positives, we additionally calculate the mean (μ) and standard deviation (σ) of time residuals (Δt) between AEsNet and analyst picks to further assess the picks precision. Arrival-time residuals Δt of less than 6.4 μs (40 samples at 6.25 MHz), are classified as true positives, with larger residuals counted as false positives.

Figure 3 shows AEsNet performance as a function of different phase score threshold values for the two tested datasets, Min-U-Sil (Figure 3A) and glass beads (Figure 3B). In both models, precision increases significantly as the threshold rises, while recall decreases, reflecting a trade-off between reducing false positives and the number of detected picks. The F1 score reaches its maximum around a threshold of 0.5 for both models, identifying it as the optimal balance between precision and recall. Thus, the 0.5 threshold was chosen for all subsequent investigations as it provides a practical compromise between accurately identifying true positives and minimizing false negatives. Importantly, the performance of the glass beads model consistently falls short compared to the Min-U-Sil model across all evaluated metrics.

Figure 4 shows how AEsNet performance varies across different signal-to-noise ratio (SNR) levels. The test set is categorized into 10 groups based on the value of ln(SNR), with precision, recall, and F1 score computed for each category. SNR is calculated as the ratio of the standard deviations of 500 samples following the P arrival (the signal) to the 500 samples preceding it (the noise). The SNR can be negative for certain AEs waveforms due to the short moveout between phase arrivals. In such cases, noise windows contain the coda of AEs that occurred before, a phenomenon particularly noticeable in glass beads waveforms.

Regarding the Min-U-Sil model (Figure 4A), performance improves as the SNR increases, with all metrics achieving higher values in the higher SNR ranges. This reflects the model's enhanced ability to accurately identify true positives when signals are clearer. Remarkably, even at very low SNR levels (<2), the model maintains solid performance, achieving an F1 score of 0.8, demonstrating its robustness under challenging conditions. On the other hand, when the SNR becomes extremely high (>8), precision drops significantly. While this might seem counterintuitive, it is attributable to the very small number of examples in this SNR bin within the training dataset (<5, right y-axis in Figure 4A). Figure 4B shows a similar trend for the testing glass beads dataset, with performance metrics improving as the SNR increases. Although the model does not perform exceptionally well, it is not entirely unreliable even at negative SNR values (<0). At higher SNR (>3.5), performance slightly declines, likely due to the scarcity of training examples in this SNR bin, consistent with the trend observed in the Min-U-Sil model. These observations highlight that the model primarily learns to identify AEs based on their unique frequency content rather than their amplitude or SNR, emphasizing the importance of having a well-distributed dataset in terms of frequency range and SNR, for robust performance.

3.2 Comparison with existing models

The performance of our AEsNet model is compared against standard picking algorithms, including the STA/LTA and AIC algorithms, both implemented in the ObsPy library Beyreuther et al. (2010). Both of these 'classic' methods for picking first arrivals require extensive user tuning, which we have attempted to optimize (Figure S1). Additionally, we benchmark our models against the Quakephase approach Shi et al. (2024). Quakephase employs advanced pre-processing techniques to improve the performance of pre-trained DL picking models on out-of-distribution datasets. Quakephase has already been tested on AEs collected during a triaxial rock deformation experiment performed on Berea sandstone samples. In our work, we apply Quakephase through Seisbench Woollam et al. (2022) by applying four different pre-trained models—the original PhaseNet, the original EQTransformer Mousavi et al. (2020), and the two models retrained on the STEAD dataset Mousavi et al. (2019). The models are applied after a series of pre-processing techniques. The first procedure involves applying a rescaling factor to the AE waveform, given by $R = t_m/t_i = s_i/s_m$, where t_m and t_i are the time window lengths of the ML model used during training and the actual input data, respectively, and s_m and s_i are the data sampling rates used for training the ML model and the designated sampling rate of the actual input data, respectively. Subsequently, bandwidth filtering is applied with a low cutoff frequency of 20 kHz and a high cutoff of 2 MHz to eliminate low-frequency noise from the hydraulic power supply and the high-frequency electrical noise that characterize our experimental data Pignalberi et al. (2024). A sliding-window approach with a an overlap ratio of 0.9 is used to enhance model performance by exposing seismic events in multiple prediction windows at different positions. The windows contain the same number of points as those used during the training of the applied DL models. At the end, the prediction results of the four different models are combined using principal component analysis (PCA), which selects the first principal component maximizing data variance as the final ensemble output. This approach automatically assigns greater weight to models with consistent predictions while downweighting outlier-like models.

Figure 5 illustrates the performance of AEsNet compared to all benchmark models across different PZTs sensor types. For Min-U-Sil (Figure 5A-B), AEsNet demonstrates robust performance across all PZTs, with F1 scores consistently exceeding 0.9. These results are significantly higher than those of the AIC, STA/LTA, and Quakephase. This last method, although showing good performance, achieved a smaller F1 score of around 0.7. An example of the picks obtained using the different tested methods for a complex Min-U-Sil waveform containing 9 AEs manually picked (marked by dashed vertical lines) is shown in Figure 6. The AIC method exhibits numerous missed picks, whereas the STA/LTA method achieves reasonable performance but introduces a noticeable delay in the automatically identified picks compared to the target picks (Figure 6C and 6D). Quakephase misses the smaller picks and often misinterprets P-wave arrivals as S-waves. AEsNet clearly outperforms all other methods, producing accurate, high-confidence picks. This strong performance is further evidenced when examining the distribution of time residuals between the automated and human-labeled P picks (Figure 5B). The residual distributions for AEsNet are noticeably narrower and show fewer biases compared to those obtained using the other methods.

Figures 5C and 5D report the same statistics for the glass beads dataset. As with the Min-U-Sil dataset, the AIC method again shows the worst performance, followed by the STA/LTA and then the DL-based methods. Despite its acceptable performance, the STA/LTA method exhibits a strongly asymmetric distribution of residuals, with picks occurring later than the true ones, indicating some bias in its predictions. Quakephase and AEsNet show very similar performance for this dataset, with AEsNet performing slightly better, particularly for SV and P sensors, as evidenced by the standard deviation (μ) of the residuals (5D). In general, SH sensors show the worst performance, which is likely related to the less sensitivity to the imposed shear direction, which favors microslip AEs with vertical directivity.

Figures S2-S3-S4-S5 show additional examples of the application of the different employed methods to AEs waveforms in the testing dataset. Figure S2 presents an example from Min-U-Sil with a low SNR of 0.7. The AIC method detects too many picks, while the STA/LTA method shows delayed picks. Quakephase and AEsNet perform similarly, with Quakephase showing slightly better residuals; however, it sometimes incorrectly interprets the P-wave first arrival as an S-wave. Figure S3 provides an example with low SNR for glass beads, where AEsNet clearly outperforms the other methods, particularly in terms of phase scores. Figure S4 highlights that AEsNet excels even in the presence of strong low-frequency background noise, which in our setup is caused by the hydraulic power supply imposing a constant normal load. AEsNet accurately detects first-arrival picks without the need for filtering, demonstrating its robustness in handling noisy conditions. Finally, Figure S5 shows an example where the amplitude of the AEs is clipped (due to exceeding the 4V voltage range), yet AEsNet successfully picks the first arrivals, further showcasing its reliability under challenging conditions.

4 Discussions

4.1 Models Generalization: How Much Training Data Is Necessary for Optimal Performance?

A major challenge in developing ML models for AE detection is the scarcity of labeled AE datasets in laboratory settings, along with the need for models capable to generalize across different experiments and conditions. Understanding how training dataset size and different experimental boundary conditions affect model performance is crucial for optimizing detection in data-limited scenarios. This section examines AEsNet's performance in relation to these factors. Regarding the Min-U-Sil dataset that includes around 16,000 training examples, QuakePhase performs reasonably well but it is significantly outperformed by AEsNet in overall accuracy and reliability. Additionally, QuakePhase faces two main challenges. First, its extensive preprocessing pipeline, including filtering, rescaling, and the aggregation of multiple DL models, although avoiding the need for hyperparameter tuning like standard picking methods, significantly slows its application Shi et al. (2024). For instance, applying AEsNet to a 1 second AE recording on a MacBook Air Pro with an Apple M1 chip takes 4 seconds, while QuakePhase (applied with only PhaseNet as the inference model and no overlapping windows and therefore we not optimal performance) takes 25 seconds. Second, QuakePhase's reliance on models trained on local natural earthquakes with clear, long (relative to window size) P-S moveouts often results in frequent misinterpretation of first-arrival AEs as S-waves.

Figure 7A shows AEsNet's performance for the different normal loads applied in the Min-U-Sil experiments present in the testing dataset. AEsNet generally shows a good generalization across different normal loads. However, performance is lower for the 10 MPa and 17 MPa loads, which have fewer training examples. It is important to note that these experiments were conducted at a sampling rate of 3.125 MHz, compared to the 6.25 MHz used for the majority of the experiments. Thus, the lower performance of AEsNet may be more attributable to the different sampling rate rather than the variation in normal load. Nevertheless, the F1 score under these conditions remains around 0.85, reflecting strong performance and significantly exceeding that achieved with Quakephase.

For the glass beads dataset, Quakephase and AEsNet perform very similarly, with reasonable performances, but never reach the very high scores of the Min-U-Sil model (Figure 5C). Why is this the case? On the one hand, this can be attributed to the lower average SNR values of glass beads AEs, which do not have very large amplitudes with respect to the noise. However, as previously demonstrated, AEsNet relies primarily on the frequency content of waveforms rather than their amplitude, which aligns with observations from the original PhaseNet model applied to natural earthquakes Zhu and Beroza (2019), and thus the less optimal performance can likely be attributed to the lower number of training examples used in training our AEsNet model.

To further investigate this, we examine the performance of the Min-U-Sil model as a function of the training dataset size, reducing it from the initial 60% (16,000 examples) to 10% (1,600 examples) in steps of 20%. The performance, along with pick time residuals, is reported in Figure 7B. As expected, reducing the number of training examples leads to a decrease in performance. However, even with a small training dataset, the Min-U-Sil AEsNet performs decently, achieving an F1 score of 0.8, still slightly better than Quakephase. This result demonstrates that with just 1,600 examples, a newly trained Min-U-Sil model can outperform the Quakephase approach. Performance is slightly lower than that achieved with the glass beads dataset, likely due to the smaller number of training examples for Min-U-Sil (2,200 vs. 1,600). To achieve a more stable model with an F1 score higher than 0.9, around 11,000 AEs examples are necessary.

Our results indicate that, in general, QuakePhase performs comparably to AEsNet for glass beads. However, for Min-U-Sil, AEsNet outperforms QuakePhase, even when a smaller training dataset is used. Additionally, QuakePhase requires longer running time and can often misinterpret P-wave first arrivals as S-wave arrivals (e.g., Figure 6). These results raise some interesting questions: why do we observe different performances for different materials? Is it possible to improve AEsNet performance with smaller AEs training datasets?

4.2 Improving Glass Beads Detection Performance: A Transfer Learning Approach

In laboratory settings we must address the challenge of a small training dataset, since the scientist must/may investigate, performing a number of experiments, different materials under different boundary condition to drive solid scientific conclusion, and does not have the possibility to manually pick thousands of waveform for each experiment. In this context, for glass beads, we attempt to apply the transfer learning technique through the use of pre-trained models. Specifically, we first apply the Min-U-Sil model and the original PhaseNet model, which was trained on natural earthquakes from the Northern California Earthquake Data Center Catalog NCEDC (2014), without any additional fine-tuning. Performance results are presented in Figure 8, which includes residuals (8A), performance metrics (8B), and phase score distributions of the transfer learning models (8C), contrasted with the glass beads AEsNet model trained from scratch whose performance has been shown in the previous sections (e.g., Figure 5C and 5D).

When applied to glass beads, the Min-U-Sil model achieves a good precision of 0.8, but the F1 score is only 0.7, indicating that it misses a significant number of picks. This lack of picking confidence is also evident in the phase score distribution (Figure 8C). Similarly, the original PhaseNet model exhibits high precision but an even lower F1 score of 0.4, highlighting the large number of missed picks. The phase scores for PhaseNet are also low, and even when applying a lower threshold, the number of detected picks remains very small. For both models, the residual distributions are skewed, with negative averages and medians, indicating that predicted picks are consistently delayed relative to the target ones. This delay may be linked to the microphysical mechanisms generating AEs in glass beads, a topic that will be explored further in the next discussion paragraph. The Min-U-Sil model, having been trained on AEs data, demonstrates reasonable performance, whereas the original PhaseNet model, trained on natural earthquakes, fails almost entirely. However, both pre-trained models generally exhibit significantly lower performance compared to the glass beads model trained from scratch.

Given the low initial performance, we further fine-tune the two pre-trained models using the glass beads training dataset. The last two columns of Figure 8 illustrate the resulting performances. Fine-tuning substantially improves the performance of both the original PhaseNet model and the retrained Min-U-Sil model, bringing them closer to the performance of the glass beads model trained from scratch. The fine-tuned PhaseNet model shows slightly lower precision, larger residuals, and marginally lower phase scores. In contrast, the retrained Min-U-Sil model outperforms the glass beads model, demonstrating higher precision, smaller residuals, and improved phase scores, indicating greater confidence in its picks.

Figure 9A shows an example of an AE from the testing dataset, along with the picks obtained with the different models. The original PhaseNet model misses all picks, while the original Min-U-Sil model identifies some false positives. The retrained models and the glass beads model trained from scratch all perform very well, with no noticeable macroscopic differences between them in this specific example.

We discuss the not exceptional results of our transfer learning exercise in the next section, where we explore the causes of this behavior and interpret the model's performance in relation to the microphysical processes driving emissions in different granular materials.

4.3 Interpreting Model Performance: Variability in AE Signatures Across Different Granular Materials

The results of our transfer learning exercise demonstrate that a model trained on natural earthquakes does not perform well when directly applied to laboratory AE data without preprocessing. Techniques like rescaling, filtering, and model aggregation used in QuakePhase can enhance performance but still present challenges. For instance, QuakePhase often misinterprets first arrivals as S-waves, and it does not perform as well as AEsNet, a model specifically trained for AEs. Interestingly, while the Min-U-Sil model performs better on glass beads than the original PhaseNet, it still falls short of optimal performance. This highlights a crucial finding: despite being trained on a large dataset, the characteristics of AEs generated by different physical mechanisms in different granular gouge materials, glass beads and Min-U-Sil, vary significantly, influencing model accuracy.

To better understand this outcome, we analyze the Power Spectral Density (PSD) of AEs waveforms for the two different materials. The PSD provides valuable insights into their distinct characteristics, as it reflects the distribution of energy across frequencies, a feature directly related to the underlying microphysical processes and source size generating AEs. Figure 10A and 10B display AE waveforms with the same amplitude for Min-U-Sil (10A) and glass beads (10B) across different piezoelectric sensors (organized by column), along with their respective PSDs (Figure 10C). Despite the similar amplitude, the difference in PSD shapes between the two materials is evident. Glass beads AEs show a much narrower frequency band where all the energy is distributed when compared with Min-U-Sil that is characterized by a much more widespread frequency range. This contrast becomes even more pronounced when examining the distribution of all normalized PSDs for all AEs in the dataset, shown for Min-U-Sil (Figure 10D) and glass beads (Figure 10E). For glass beads, the median PSD exhibits a relatively evident concentration in the mid-frequency range (150-500kHz), with two evident picks, followed by a gradual, almost linear decline as the frequency increases. Conversely, the Min-U-Sil PSD spans a much broader frequency range. The median PSD shows a higher concentration of energy at lower frequencies compared to glass beads, followed by an energy plateau that declines more steeply at higher frequencies (>1 MHz), culminating in a prominent high-frequency bump, appearing around 1 MHz. The distinct frequency content of AEs generated by glass beads and Min-U-Sil reflects their different deformation mechanisms. The deformation in glass beads is fundamentally governed by the physics of force chains—a network of interconnected particles that transmit concentrated stress or force along specific paths through the system Morgan and Boettcher (1999), Johnson et al. (2013), Ferdowsi et al. (2013), Scuderi et al. (2015). AEs predominantly correspond to the volumetric breaking of force chains, which, under the low normal stress experimental conditions we tested, do not involve the breakage and comminution of single beads Mair et al. (2002). The maximum size of force chains, and consequently of AE sources, is inherently dictated by the gouge layer thickness (3 mm) (Anthony and Marone (2005). Since frequencies are, to a first approximation, inversely proportional to seismic source size, this limitation likely explains the sharp drop in AE frequencies below 100 kHz, which reflects the largest force chain that can form within the layer. In contrast, in Min-U-Sil, deformation is dominated by shear localization, marked by the formation of localized slipping planes parallel to the imposed shear that accommodate most of the accumulated strain energy forming by micro-physical processes such as grain comminution, breakage and micro-slips. AEs in this material exhibit higher energy at lower frequencies, indicating larger seismic sources compared to glass beads. These events are likely associated with the failure of millimeter- to centimeter-sized asperities along the localized slipping surfaces, as evidenced by AE location data Trugman et al. (2020), frequency content analysis Bolton et al. (2020, 2022), waveform similarities Bolton et al. (2023), seismic source spectral estimates Pignalberi et al. (2024), active acoustic imaging Shreedharan et al. (2020), and microstructural observations Scuderi et al. (2017). AEs in Min-U-Sil can involve ruptures spanning the entire sample plane, potentially reaching the full sample size of 5 cm, resulting in larger seismic sources and broader frequency content. Additionally, AEs generated in Min-U-Sil exhibit more pronounced high-frequency content than those in glass beads, a feature attributed to Min-U-Sil's smaller grain size and linked to brittle processes, including microcracking, grain size reduction, and cataclastic activity **?**. Such processes collectively shape the broader and more complex PSD of the AEs in Min-U-Sil. Specifically, AEs in glass beads lack the high-frequency signatures typically associated with asperity-scale shear rupture processes, which are usually contained within the first microsecond of AE waveforms Bolton et al. (2023). The differences in PSD shapes also explain the tendency of the Min-U-Sil model to detect AEs with a delay when applied to glass beads (see picks residuals in Figure 8A). Our PSD analysis highlights the unique acoustic signatures of the two materials, underscoring their distinct frequency characteristics shaped by their mechanical and microphysical deformation processes.

5 Conclusion

In this study, we introduce AEsNet, a PhaseNet-based picker designed to detect AEs generated during laboratory experiments from two different granular materials: Min-U-Sil and glass beads. We demonstrate its superior performance compared to all previously existing picking methods, including other DL models trained on natural earthquakes. AEsNet achieves better results for Min-U-Sil than for glass beads, reflecting the impact of training dataset size. Our findings suggest that picking performance is influenced by the number of training examples and is primarily driven by the signal frequency content, rather than their absolute amplitude or SNR, highlighting the importance of the physics of the source properties.

When transfer learning is applied to address the limited dataset size for glass beads, the model's reliance on frequency content becomes even more evident. Applying the Min-U-Sil model to glass beads yields unsatisfactory performance, underscoring the strong dependence of picker models on the specific granular material they are trained on, particularly the microphysical processes generating AEs. This observation aligns with findings from DL pickers for natural earthquakes. While such models can sometimes be successfully transferred to different regions of the world Cianetti et al. (2021), they often exhibit performance degradation when generalized across distinct tectonic settings. Furthermore, these models typically perform poorly when applied to datasets involving significant changes in scale, such as transferring between regional and teleseismic distances Münchmeyer et al. (2022). This underscores the importance of adapting picker models to the specific characteristics of the seismic signals and environments they are intended to analyze, whether for natural earthquakes or laboratory AEs. Additional fine-tuning can significantly enhance the performance of pre-trained models and is often necessary for specific environments, as has been observed for seismic signals collected in Antarctica Ho et al. (2024).

In our experiments, retraining the Min-U-Sil model on the glass beads dataset resulted in significantly improved performance. Despite the distinct micromechanical processes generating AEs in these materials, our results indicate that fine-tuning a model pre-trained on Min-U-Sil AEs performs better at detecting AEs in glass beads than using a fine-tuned model pre-trained on natural earthquake data, even when the latter is trained on a substantially larger dataset. This finding highlights that, while preprocessing techniques such as rescaling can improve the performance of earthquake pickers on AEs data, inherent temporal differences between AEs and natural earthquakes critically influence AEs picker performance. Importantly, our findings highlight that training a new PhaseNet model for AE detection does not require large datasets; just a few thousand waveforms are sufficient, and potential fine-tuning can further reduce this requirement, making it a practical and efficient strategy for AE detection across diverse laboratory conditions. This aligns with the findings of Chai et al. (2020), who successfully adapted the original PhaseNet model, trained on local seismic data, for mesoscale hydraulic fracturing experiments. Their study showed that only a few thousand waveforms were sufficient to bridge the three orders of magnitude difference in both spatial and temporal scales between the original training data and the target data. In conclusion, our approach provides a flexible, robust and fast framework for enhancing AE detection, even with limited datasets from diverse laboratory conditions. This capability enables the rapid generation of reliable AE catalogs, offering critical insights into fault micromechanics and potential applications for understanding fault behavior in natural settings.

Data and Resources

The supplementary figures are provided in the Supporting Information file. The dataset used in this study, along with the trained models and a Jupyter notebook for reproducing the figures presented in the paper, is available at https://zenodo.org/records/14639594. The complete codebase will be made available on GitHub upon publication. The GitHub repository will also include explanatory Jupyter notebooks demonstrating how to use our models and train new models from scratch.

Acknowledgments

This research was funded by European Research Council ERC g.a. n.o. 101040600 (HYQUAKE) to MMS and PRIN giovani PREVENT to MMS. We thank Luca Coppola, Aurora Perrella, Michele De Solda, Giovanni Guglielmi, and Michele Mauro for their valuable contributions in manually picking many AE waveforms.

Declaration of Competing Interests

The authors declare that they have no known competing financial interests or personal relationships that could have appeared to influence the work reported in this paper.

References

Allen, R. (1978). Automatic earthquake recognition and timing from single traces. *Bulletin of the Seismological Society of America*, 68(5):1521–1532.

Anthony, J. L. and Marone, C. (2005). Influence of particle characteristics on granular friction. *Journal of Geophysical Research: Solid Earth*, 110(B8).

Bedford, J. D. and Faulkner, D. R. (2021). The role of grain size and effective normal stress on localization and the frictional stability of simulated quartz gouge. *Geophysical Research Letters*, 48:e2020GL092023.

Beyreuther, M., Barsch, R., Krischer, L., Megies, T., Behr, Y., and Wassermann, J. (2010). Obspy: A python toolbox for seismology. *Seismological Research Letters*, 81(3):530–533.

Blanke, A., Kwiatek, G., Goebel, T. H. W., Bohnhoff, M., and Dresen, G. (2021). Stress drop–magnitude dependence of acoustic emissions during laboratory stick-slip. *Geophysical Journal International*, 224(2):1371–1380.

Bolton, D. C., Marone, C., Saffer, D., and Trugman, D. (2023). Foreshock properties illuminate nucleation processes of slow and fast laboratory earthquakes. *Nature Communications*, 14:3859.

Bolton, D. C., Shreedharan, S., McLaskey, G. C., Rivière, J., Shokouhi, P., Trugman, D. T., and Marone, C. (2022). The high-frequency signature of slow and fast laboratory earthquakes. *Journal of Geophysical Research: Solid Earth*, 127:e2022JB024170.

Bolton, D. C., Shreedharan, S., Rivière, J., and Marone, C. (2020). Acoustic energy release during the laboratory seismic cycle: Insights on laboratory earthquake precursors and prediction. *Journal of Geophysical Research: Solid Earth*, 125:e2019JB018975.

Bolton, D. C., Shreedharan, S., Rivière, J., and Marone, C. (2021). Frequency-magnitude statistics of laboratory foreshocks vary with shear velocity, fault slip rate, and shear stress. *Journal of Geophysical Research: Solid Earth*, 126:e2021JB022175.

Chai, C., Maceira, M., Santos-Villalobos, H. J., Venkatakrishnan, S. V., Schoenball, M., Zhu, W., et al. (2020). Using a deep neural network and transfer learning to bridge scales for seismic phase picking. *Geophysical Research Letters*, 47:e2020GL088651.

Cianetti, S., Bruni, R., Gaviano, S., Keir, D., Piccinini, D., Saccorotti, G., and Giunchi, C. (2021). Comparison of deep learning techniques for the investigation of a seismic sequence: An application to the 2019, mw 4.5 mugello (italy) earthquake. *Journal of Geophysical Research: Solid Earth*, 126:e2021JB023405.

Dresen, G., Kwiatek, G., Goebel, T., et al. (2020). Seismic and aseismic preparatory processes before large stick–slip failure. *Pure and Applied Geophysics*, 177:5741–5760.

Ferdowsi, B., Griffa, M., Guyer, R. A., Johnson, P. A., Marone, C., and Carmeliet, J. (2013). Microslips as precursors of large slip events in the stick-slip dynamics of sheared granular layers: A discrete element model analysis. *Geophysical Research Letters*, 40(16):4194–4198.

Goebel, T. H., Kwiatek, G., Becker, T. W., Brodsky, E. E., and Dresen, G. (2017). What allows seismic events to grow big?: Insights from b-value and fault roughness analysis in laboratory stick-slip experiments. *Geology*, 45:815–818.

Goebel, T. H. W., Schorlemmer, D., Becker, T. W., Dresen, G., and Sammis, C. G. (2013). Acoustic emissions document stress changes over many seismic cycles in stick-slip experiments. *Geophysical Research Letters*, 40:2049–2054.

Goebel, T. H. W., Schuster, V., Kwiatek, G., et al. (2024). A laboratory perspective on accelerating preparatory processes before earthquakes and implications for foreshock detectability. *Nature Communications*, 15:5588.

Goodfellow, S. D. and Young, R. P. (2014). A laboratory acoustic emission experiment under in situ conditions. *Geophysical Research Letters*, 41(10):3422–3430.

Gutenberg, B. and Richter, C. F. (1944). Frequency of earthquakes in california. *Bulletin of the Seismological Society of America*, 34(4):185–188.

Heimann, S., Kriegerowski, M., Isken, M., et al. (2017). Pyrocko - an open-source seismology toolbox and library. *GFZ Data Services*.

Ho, L. M., Walter, J. I., Hansen, S. E., Sánchez-Roldán, J. L., and Peng, Z. (2024). Evaluating automated seismic event detection approaches: An application to victoria land, east antarctica. *Journal of Geophysical Research: Machine Learning and Computation*, 1:e2024JH000185.

Hulbert, C., Rouet-Leduc, B., Johnson, P., et al. (2019). Similarity of fast and slow earthquakes illuminated by machine learning. *Nature Geoscience*, 12:69–74.

Johnson, P. A., Ferdowsi, B., Kaproth, B. M., et al. (2013). Acoustic emission and microslip precursors to stick-slip failure in sheared granular material. *Geophysical Research Letters*, 40:5627–5631.

Karimpouli, S., Caus, D., Grover, H., Martínez-Garzón, P., Bohnhoff, M., Beroza, G. C., Dresen, G., Goebel, T., Weigel, T., and Kwiatek, G. (2023). Explainable machine learning for labquake prediction using catalog-driven features. *Earth and Planetary Science Letters*, 622:118383.

Korkolis, E., Niemeijer, A. R., Paulssen, H., and Trampert, J. (2021). A laboratory perspective on the gutenberg-richter and characteristic earthquake models. *Journal of Geophysical Research: Solid Earth*, 126(8):e2021JB021730. e2021JB021730 2021JB021730.

Kwiatek, G., Goebel, T. H. W., and Dresen, G. (2014). Seismic moment tensor and b value variations over multiple seismic cycles in laboratory stick-slip experiments. *Geophysical Journal International*, 198:273–286.

Kwiatek, G., Martínez-Garzón, P., Goebel, T., Bohnhoff, M., Ben-Zion, Y., and Dresen, G. (2024). Intermittent criticality multi-scale processes leading to large slip events on rough laboratory faults. *Journal of Geophysical Research: Solid Earth*, 129:e2023JB028411.

Leeman, J., Saffer, D., and Scuderi, M. e. a. (2016). Laboratory observations of slow earthquakes and the spectrum of tectonic fault slip modes. *Nature Communications*, 7:11104.

Lei, X. and Ma, S. (2014). Laboratory acoustic emission study for earthquake generation process. *Earthquake Science*, 27:627–646.

Lockner, D., Byerlee, J., and Kuksenko, V. e. a. (1991). Quasi-static fault growth and shear fracture energy in granite. *Nature*, 350:39–42.

Lubbers, N. E., Bolton, D. C., Mohd-Yusof, J., Marone, C., Barros, K. M., and Johnson, P. A. (2018). Earthquake catalog-based machine learning identification of laboratory fault states and the effects of magnitude of completeness. *Geophysical Research Letters*, 45:13269–13276.

Main, I. G. (1992). Damage mechanics with long-range interactions: Correlation between the seismic b-value and the fractal two-point correlation dimension. *Geophysical Journal International*, 111(3):531–541.

Main, I. G., Meredith, P. G., and Jones, C. (1989). A reinterpretation of the precursory seismic b-value anomaly from fracture mechanics. *Geophysical Journal International*, 96:131–138.

Mair, K., Frye, K. M., and Marone, C. (2002). Influence of grain characteristics on the friction of granular shear zones. *Journal of Geophysical Research: Solid Earth*, 107(B10):ECV 4–1–ECV 4–9.

Marty, S., Schubnel, A., Bhat, H. S., J., E., and Latour, S. (2023). Nucleation of laboratory earthquakes: Quantitative analysis and scalings. *Journal of Geophysical Research: Solid Earth*, 128:e2022JB026294.

McLaskey, G. and Glaser, S. (2012). Acoustic emission sensor calibration for absolute source measurements. *Journal of Nondestructive Evaluation*, 31:157–168.

McLaskey, G. C. and Kilgore, B. D. (2013). Foreshocks during the nucleation of stick-slip instability. *Journal of Geophysical Research: Solid Earth*, 118:2982–2997.

McLaskey, G. C., Lockner, D. A., Kilgore, B. D., and Beeler, N. M. (2015). A robust calibration technique for acoustic emission systems based on momentum transfer from a ball drop. *Bulletin of the Seismological Society of America*, 105(1):257–271.

Mogi, K. (1962). Study of elastic shocks caused by the fracture of heterogeneous materials and its relations to earthquake phenomena. *Bulletin of the Earthquake Research Institute, University of Tokyo*, 40:125–173.

Mogi, K. (1966). Earthquakes and fractures. *Tectonophysics*, 5(3):1–8.

Morgan, J. K. and Boettcher, M. S. (1999). Numerical simulations of granular shear zones using the distinct element method: 1. shear zone kinematics and the micromechanics of localization. *Journal of Geophysical Research: Solid Earth*, 104(B2):2703–2719.

Mousavi, S. M., Ellsworth, W. L., Zhu, W., Chuang, L. Y., and Beroza, G. C. (2020). Earthquake transformer—an attentive deep-learning model for simultaneous earthquake detection and phase picking. *Nature Communications*, 11:3952.

Mousavi, S. M., Sheng, Y., Zhu, W., and Beroza, G. C. (2019). Stanford earthquake dataset (stead): A global data set of seismic signals for ai. *IEEE Access*.

Münchmeyer, J., Woollam, J., Rietbrock, A., Tilmann, F., Lange, D., Bornstein, T., et al. (2022). Which picker fits my data? a quantitative evaluation of deep learning based seismic pickers. *Journal of Geophysical Research: Solid Earth*, 127:e2021JB023499.

NCEDC (2014). Northern california earthquake data center. Dataset, UC Berkeley Seismological Laboratory.

Omori, F. (1894). On after-shocks of earthquakes. *Journal of the College of Science, Imperial University of Tokyo*, 7:111–200.

Perol, T., Gharbi, M., and Denolle, M. (2018). Convolutional neural network for earthquake detection and location. *Science Advances*, 4(2):e1700578.

Pignalberi, F., Mastella, G., Giorgetti, C., and Scuderi, M. M. (2024). Estimating lab-quake source parameters: Spectral inversion from a calibrated acoustic system. *Sensors*, 24:5824.

Rivière, J., Lv, Z., Johnson, P. A., and Marone, C. (2018). Evolution of b-value during the seismic cycle: Insights from laboratory experiments on simulated faults. *Earth and Planetary Science Letters*, 482:407–413.

Ronneberger, O., Fischer, P., and Brox, T. (2015). U-net: Convolutional networks for biomedical image segmentation. In Navab, N., Hornegger, J., Wells, W. M., and Frangi, A. F., editors, *Medical Image Computing and Computer-Assisted Intervention – MICCAI 2015*, pages 234–241, Cham. Springer International Publishing.

Ross, Z. E., Meier, M., Hauksson, E., and Heaton, T. H. (2018). Generalized seismic phase detection with deep learning. *Bulletin of the Seismological Society of America*, 108(5A):2894–2901.

Rouet-Leduc, B., Hulbert, C., Bolton, D. C., Ren, C. X., Riviere, J., Marone, C., and Johnson, P. A. (2018). Estimating fault friction from seismic signals in the laboratory. *Geophysical Research Letters*, 45:1321–1329.

Rouet-Leduc, B., Hulbert, C., Lubbers, N., Barros, K., Humphreys, C. J., and Johnson, P. A. (2017). Machine learning predicts laboratory earthquakes. *Geophysical Research Letters*, 44(18):9276–9282.

Scholz, C. H. (1968). The frequency-magnitude relation of microfracturing in rock and its relation to earthquakes. *Bulletin of the Seismological Society of America*, 58(1):399–415.

Scuderi, M., Collettini, C., Viti, C., Tinti, E., and Marone, C. (2017). Evolution of shear fabric in granular fault gouge from stable sliding to stick slip and implications for fault slip mode. *Geology*, 45(8):731–734.

Scuderi, M. M., Carpenter, B. M., Johnson, P. A., and Marone, C. (2015). Poromechanics of stick-slip frictional sliding and strength recovery on tectonic faults. *Journal of Geophysical Research: Solid Earth*, 120(10):6895–6912.

Scuderi, M. M., Carpenter, B. M., and Marone, C. (2014). Physicochemical processes of frictional healing: Effects of water on stick-slip stress drop and friction of granular fault gouge. *Journal of Geophysical Research: Solid Earth*, 119(5):4090–4105.

Selvadurai, P. A. (2019). Laboratory insight into seismic estimates of energy partitioning during dynamic rupture: An observable scaling breakdown. *Journal of Geophysical Research: Solid Earth*, 124(11):11350–11379.

Shi, P., Meier, M.-A., Villiger, L., Tuinstra, K., Selvadurai, P. A., Lanza, F., Yuan, S., Obermann, A., Mesimeri, M., Münchmeyer, J., Bianchi, P., and Wiemer, S. (2024). From labquakes to megathrusts: Scaling deep learning based pickers over 15 orders of magnitude. *Journal of Geophysical Research: Machine Learning and Computation*, 1(4):e2024JH000220.

Shreedharan, S., Bolton, D. C., Rivière, J., and Marone, C. (2020). Preseismic fault creep and elastic wave amplitude precursors scale with lab earthquake magnitude for the continuum of tectonic failure modes. *Geophysical Research Letters*, 46.

Shreedharan, S., Rivière, J., Bhattacharya, P., and Marone, C. (2019). Frictional state evolution during normal stress perturbations probed with ultrasonic waves. *Journal of Geophysical Research: Solid Earth*, 124:5469–5491.

Sleeman, R. and Van Eck, T. (1999). Robust automatic p-phase picking: An on-line implementation in the analysis of broadband seismogram recordings. *Physics of the Earth and Planetary Interiors*, 113:265–275.

Soto, H. and Schurr, B. (2021). Deepphasepick: A method for detecting and picking seismic phases from local earthquakes based on highly optimized convolutional and recurrent deep neural networks. *Geophysical Journal International*, 227(2):1268–1294.

Tan, Y. J., Waldhauser, F., Ellsworth, W. L., Zhang, M., Zhu, W., Michele, M., Chiaraluce, L., Beroza, G. C., and Segou, M. (2021). Machine-learning-based high-resolution earthquake catalog reveals how complex fault structures were activated during the 2016–2017 central italy sequence. *The Seismic Record*, 1(1):11–19.

Trugman, D. T., McBrearty, I. W., Bolton, D. C., Guyer, R. A., Marone, C., and Johnson, P. A. (2020). The spatiotemporal evolution of granular microslip precursors to laboratory earthquakes. *Geophysical Research Letters*, 47:e2020GL088404.

Wang, K., Johnson, C. W., Bennett, K. C., and Johnson, P. A. (2022). Predicting future laboratory fault friction through deep learning transformer models. *Geophysical Research Letters*, 49(19):e2022GL098233. e2022GL098233 2022GL098233.

Woollam, J., Münchmeyer, J., Tilmann, F., Rietbrock, A., Lange, D., Bornstein, T., et al. (2022). Seisbench—a toolbox for machine learning in seismology. *Seismological Research Letters*, 93(3):1695–1709.

Zhu, W. and Beroza, G. C. (2019). Phasenet: A deep-neural-network-based seismic arrival-time picking method. *Geophysical Journal International*, 216(1):261–273.

Zhu, W., Tai, K. S., Mousavi, S. M., Bailis, P., and Beroza, G. C. (2022). An end-to-end earthquake detection method for joint phase picking and association using deep learning. *Journal of Geophysical Research: Solid Earth*, 127(3):e2021JB023283. e2021JB023283 2021JB023283.

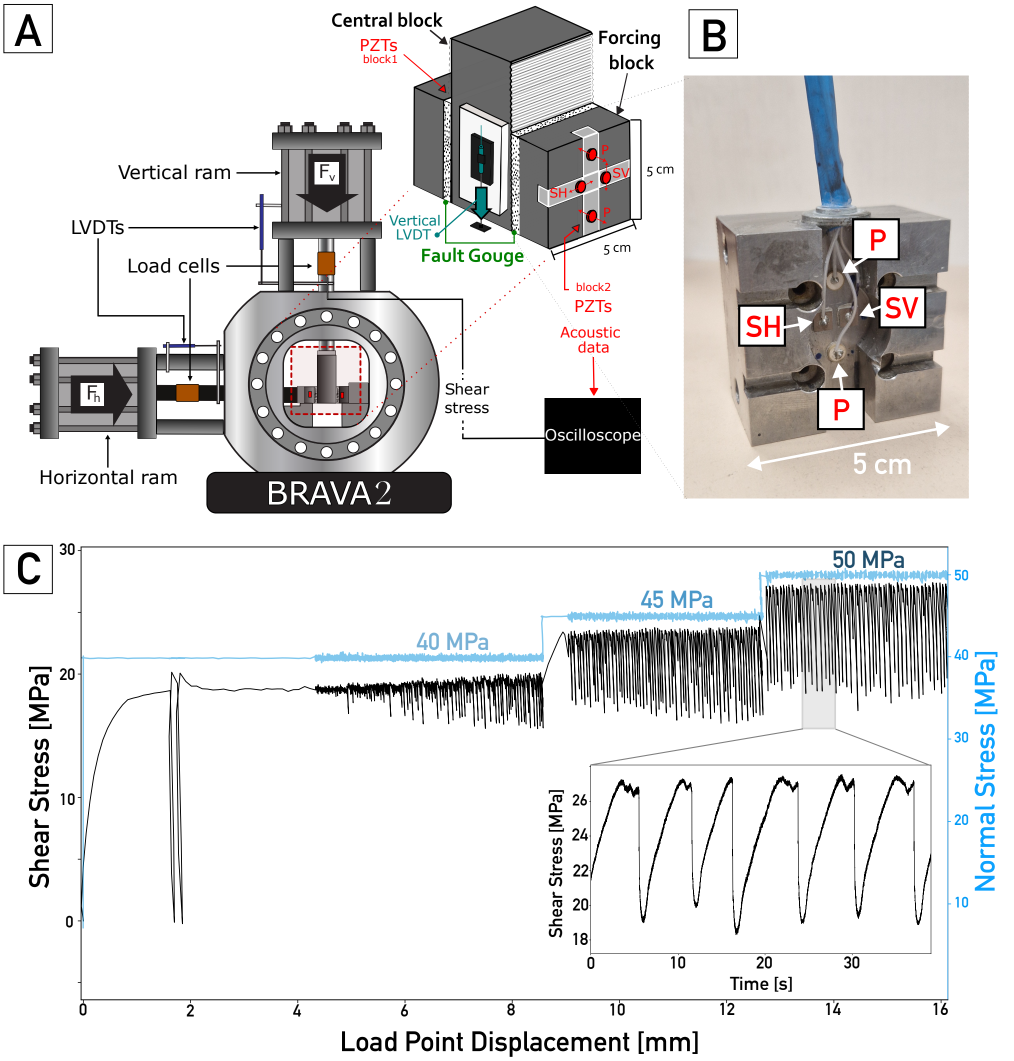

Figure 1: (A) The BRAVA2 biaxial apparatus. (B) Rear view of the side blocks showing the piezoelectric sensor positions. (C) Shear stress-displacement curve for a laboratory experiment using Min-U-Sil as the fault shearing material at different normal stress values. The inset on the right shows a zoomed-in view of some seismic cycles.

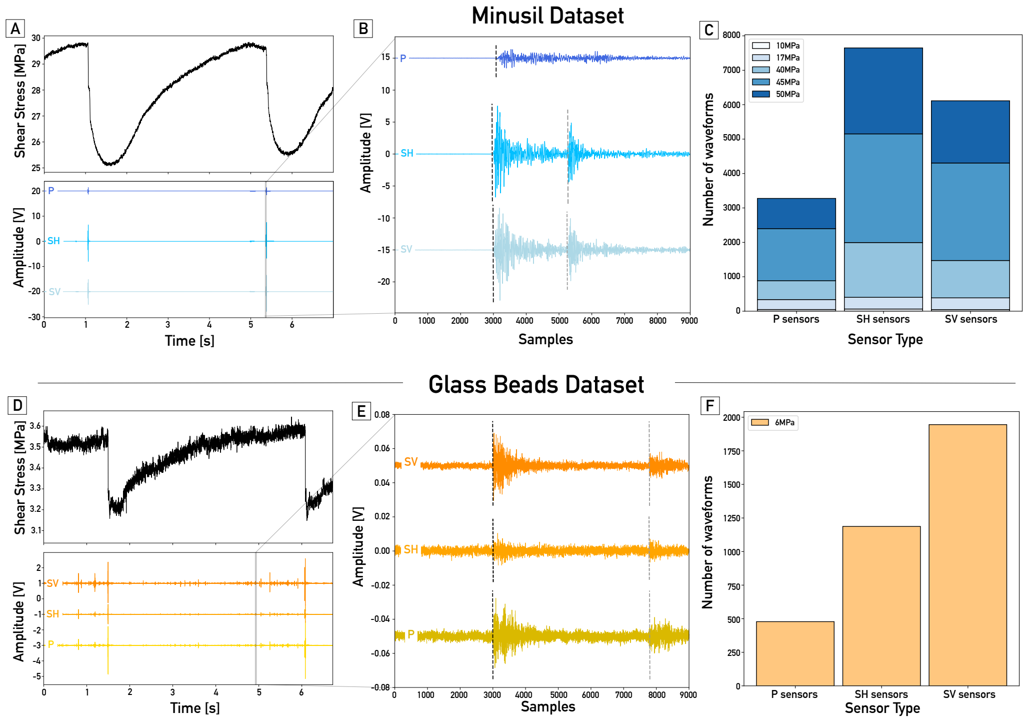

Figure 2: Experimental data and waveform distribution for the Min-U-Sil (A-B-C) and glass beads (D-E-F) datasets. Panels A and D depict the shear stress evolution alongside continuous AE activity recorded by three piezoelectric sensors (P, SH, and SV). Panels B and E provide a zoomed-in view of the acoustic data, showing an example waveform used for training AEsNet, where vertical dashed lines represent the manual target picks. Panel C and F illustrates the distribution of AE waveforms, categorized by material, applied normal stress, and sensor type.

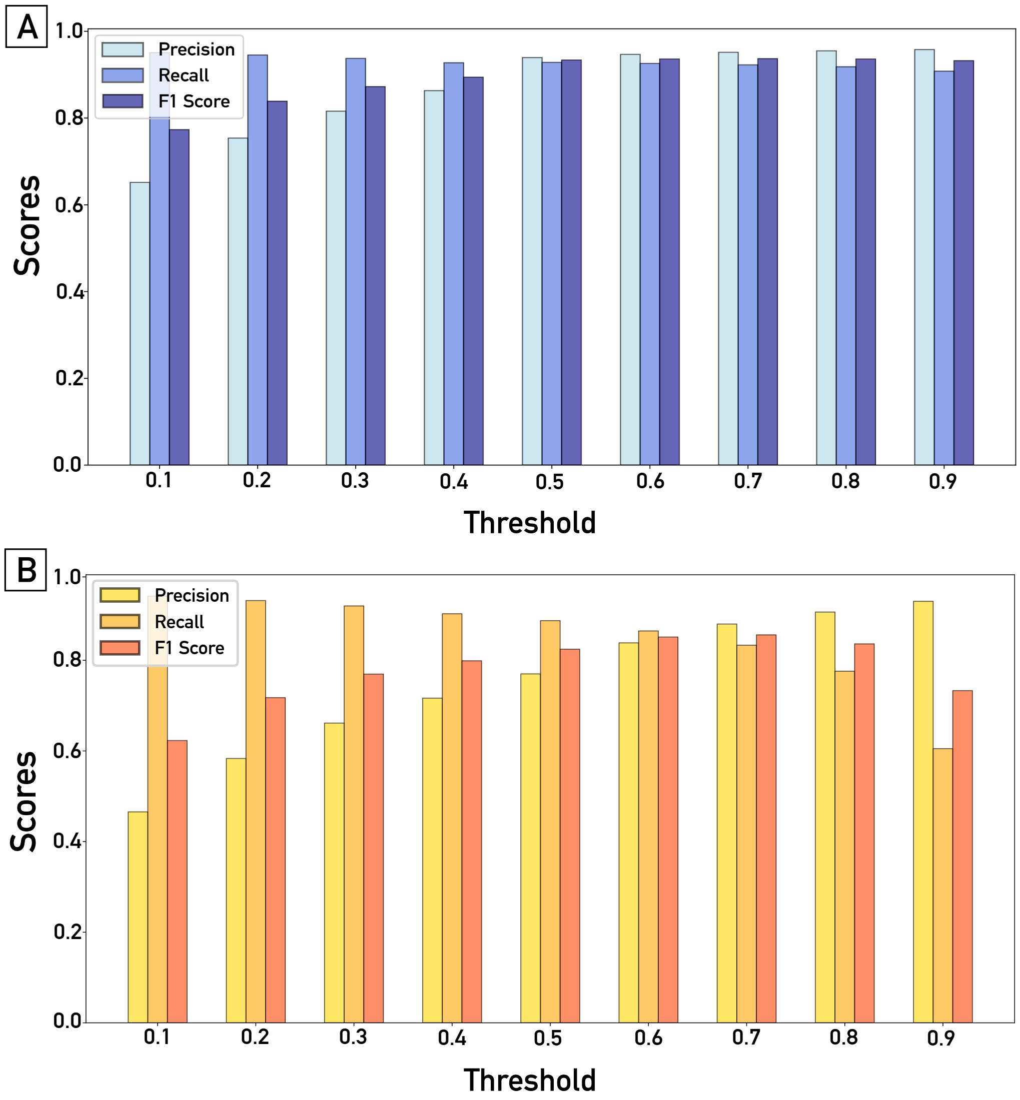

Figure 3: Performance of AEsNet on the testing dataset as a function of the phase score threshold used to extract picks from output probabilities for Min-U-Sil (A) and glass beads (B).

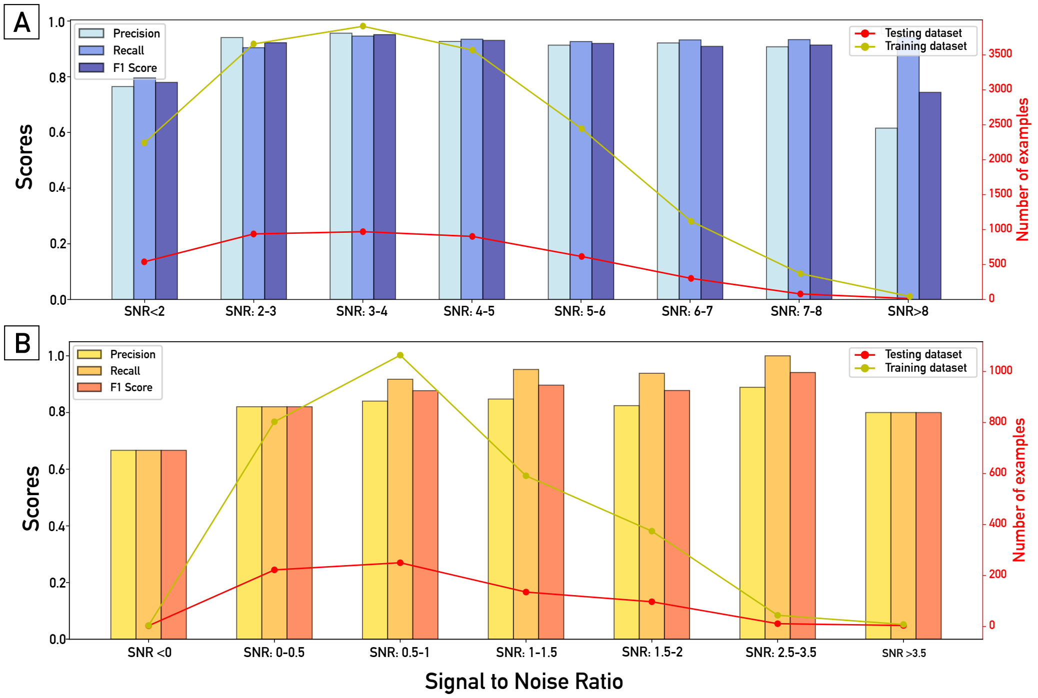

Figure 4: Performance of AEsNet on the testing dataset and number of examples in the training and testing datasets across different signal-to-noise ratios for Min-U-Sil (A) and glass beads (B).

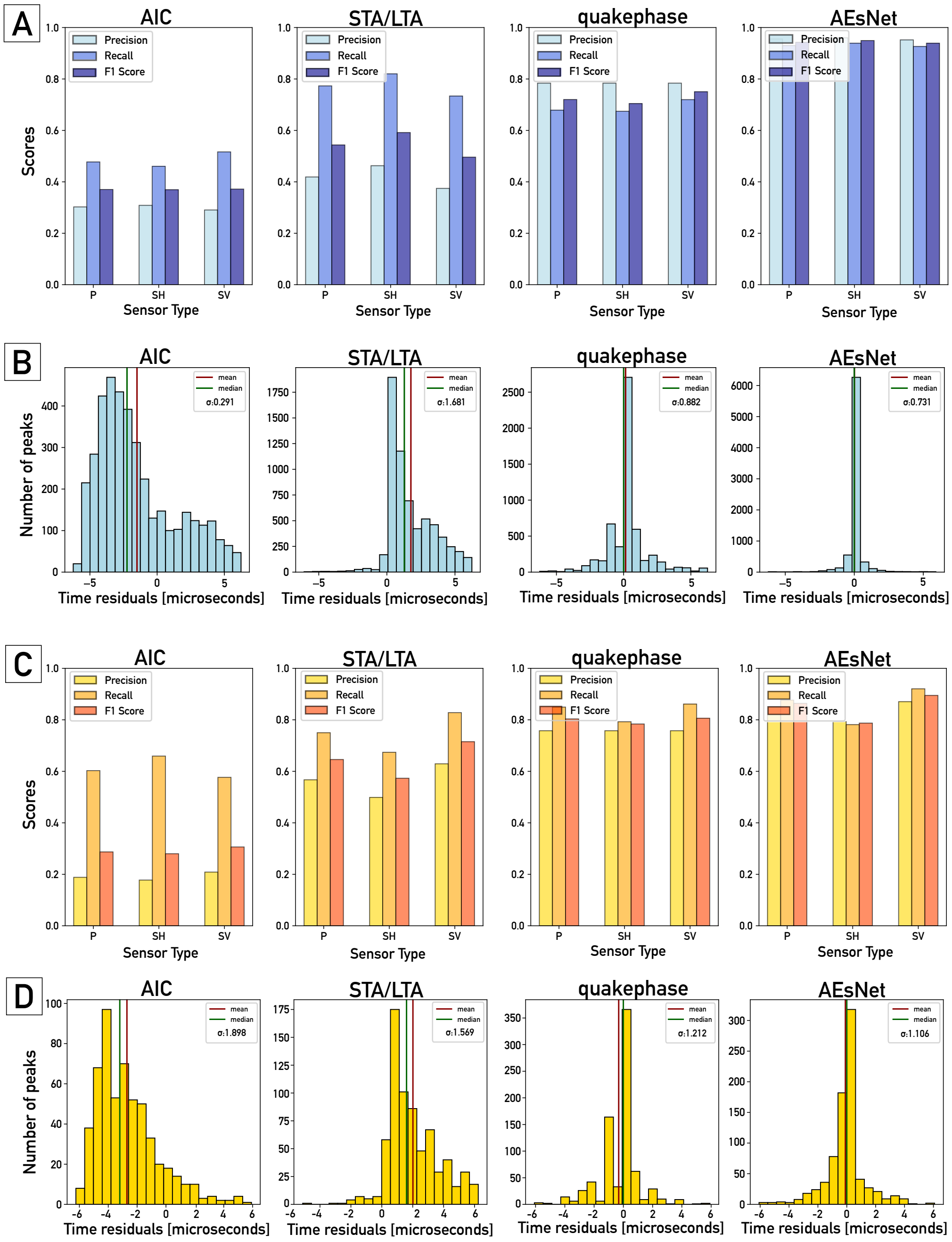
A
B
C
D
AIC
STA/LTA
quakephase
AEsNet
Precision
Recall
F1 Score
Scores
Sensor Type
P
SH
SV
Number of peaks
Time residuals [microseconds]
mean
median
σ:0.291
σ:1.681
σ:0.882
σ:0.731
σ:1.898
σ:1.569
σ:1.212
σ:1.106

Figure 5: Benmarching AEsNet performance. Precision, recall, and F1 score of each picking method (AIC, STA/LTA, Quakephase, and AEsNet) across different piezoelectric sensor types (P, SH, and SV) are shown for Min-U-Sil (A) and glass beads (C). Distributions of time residuals for each picking method are presented for Min-U-Sil (B) and glass beads (D). AEsNet consistently outperforms the other benchmark methods for the Min-U-Sil dataset, while for glass beads, it only slightly outperforms Quakephase.

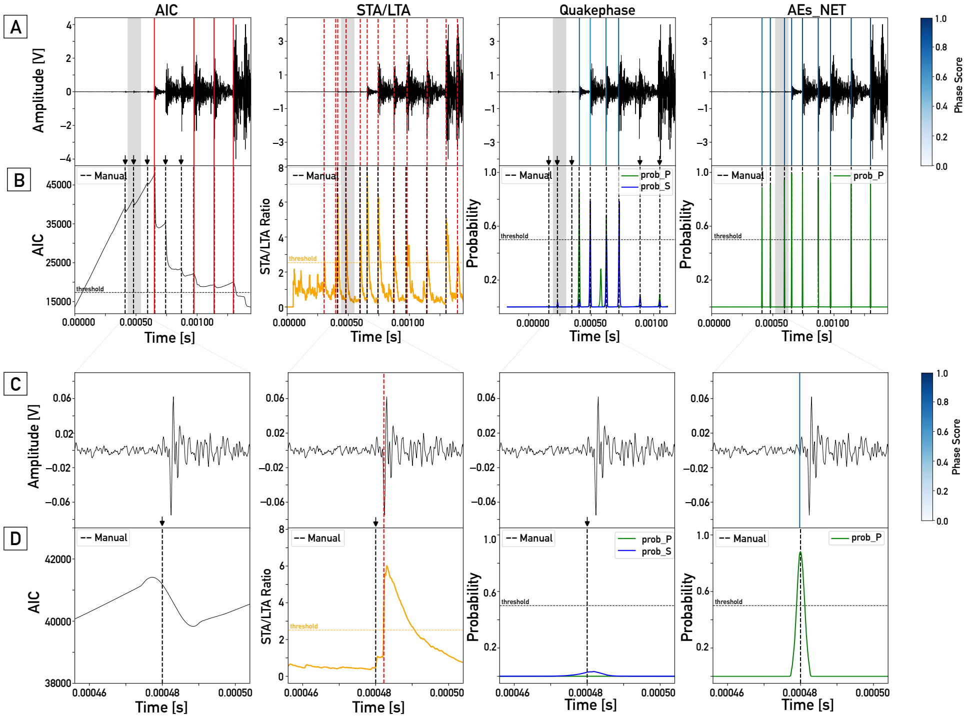

Figure 6: Comparison of Picking Methods on Min-U-Sil testing Dataset. (A) Examples of picks obtained from different methods for a challenging waveform with nine AEs (dashed black vertical lines). The raw waveform is shown in Panel (A), with a zoomed view presented in (C). Panel (B) displays the output probabilities, with a detailed zoom shown in (D). Black arrows highlight missed picks. The AIC method misses many picks, while STA/LTA produces delayed picks relative to the targets. Quakephase struggles to detect smaller picks and often misinterprets P-wave arrivals as S-waves. In contrast, AEsNet demonstrates superior performance, delivering accurate and high-confidence picks.

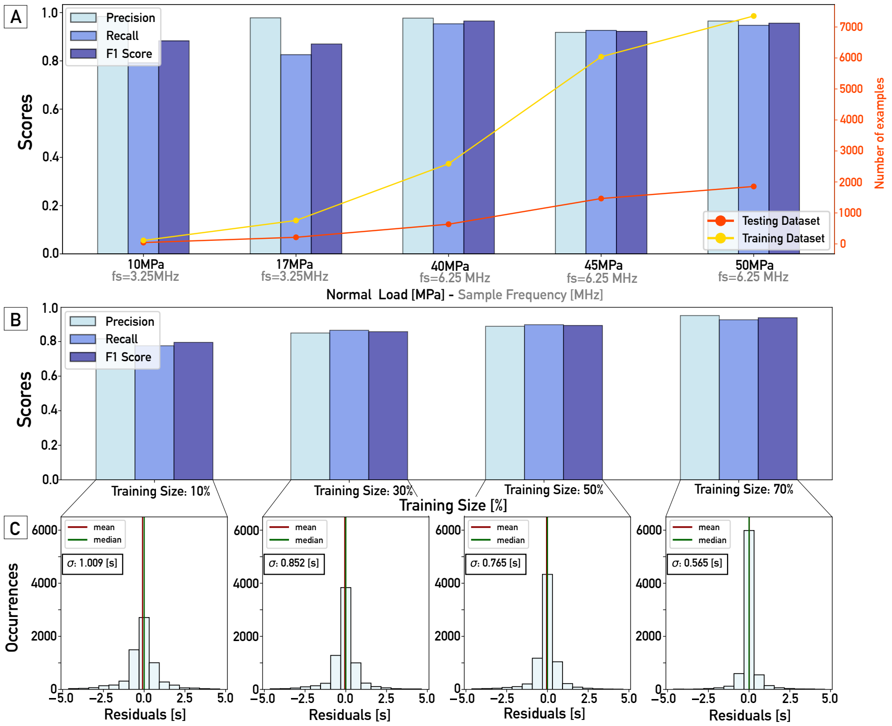

Figure 7: Analyzing the Generalizability of AEsNet on the Min-U-Sil Dataset. (A) Performance of AEsNet in terms of precision, recall, and F1 score in the testing dataset, and number of examples in the training and testing datasets across different normal loads and sampling frequencies. Lower performance is observed for 10 MPa and 17 MPa, likely due to fewer training examples and a lower sampling frequency (3.125 MHz) compared to 6.25 MHz for most other loads. (B) Performance of AEsNet and residual distributions for different training dataset sizes, ranging from 10 % to 70 %, illustrating the impact of dataset size on AEsNet's performance and generalizability.

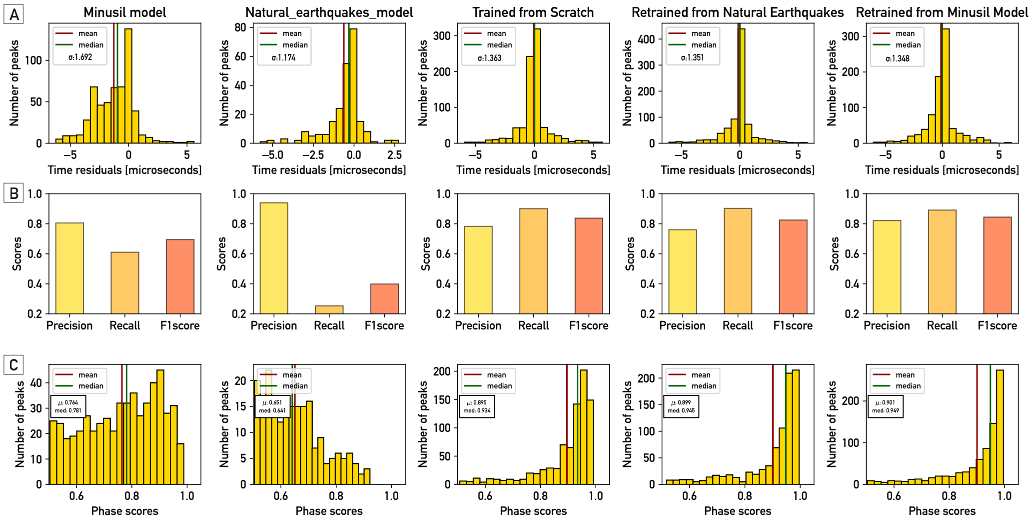

Figure 8: Performance of various DL models on the Glass Beads testing dataset. Panel (A) displays the residual distributions of predicted picks relative to manual picks for five models: the Min-U-Sil model, the original PhaseNet model trained on natural earthquakes, the glass beads model trained from scratch, and two fine-tuned models (Min-U-Sil retrained on glass beads and PhaseNet retrained on glass beads). Mean and median residuals are indicated for each distribution. Panel (B) presents precision, recall, and F1 score metrics for each model, showing that fine-tuned models achieve significantly improved performance. Panel (C) illustrates phase score distributions, highlighting the confidence of picks made by each model. In general, retraining the Min-U-Sil model on glass beads yields optimal performance.

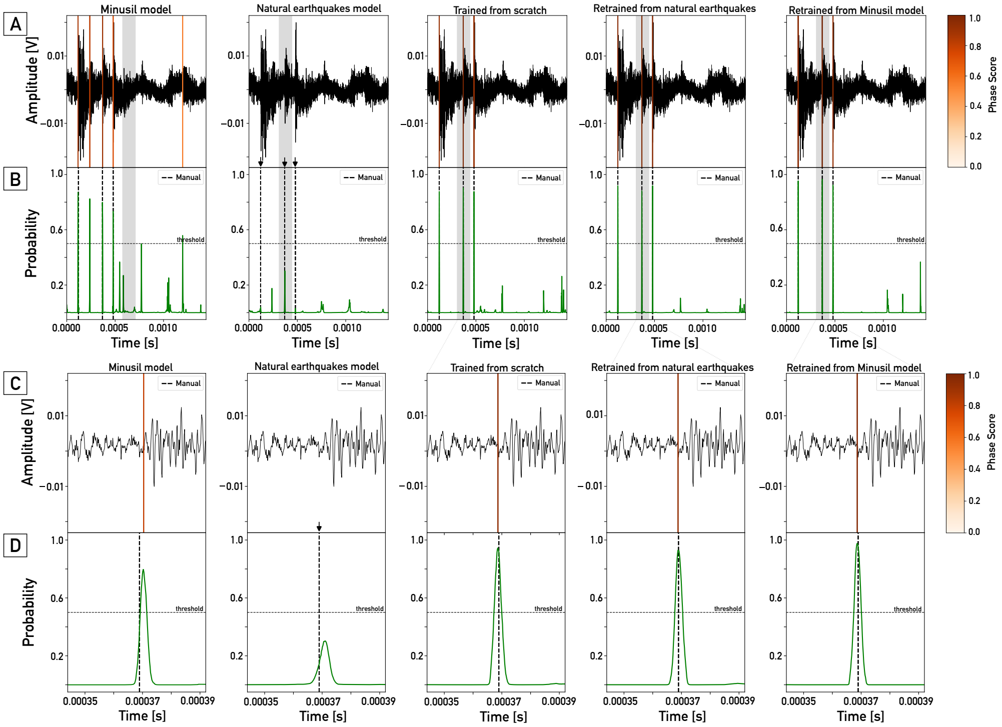

Figure 9: Example of AE waveform from the glass beads testing dataset, comparing picks obtained using different DL models. Panel (A) represents the raw waveform, with a zoom presented in (C). Panel (B) shows the output probabilities, with a zoom provided in (D). Manual picks are displayed as dashed black lines. Extracted picks are those with a phase score higher than 0.5. Black arrows highlight missed peaks. The original PhaseNet model trained on natural earthquakes demonstrates poor performance, missing many picks. The Min-U-Sil model identifies some false positives but provides better results. Fine-tuned models, including those retrained from the original PhaseNet and Min-U-Sil models, achieve significantly improved performance. These models produce accurate picks with high confidence, similar to the glass beads model trained from scratch.

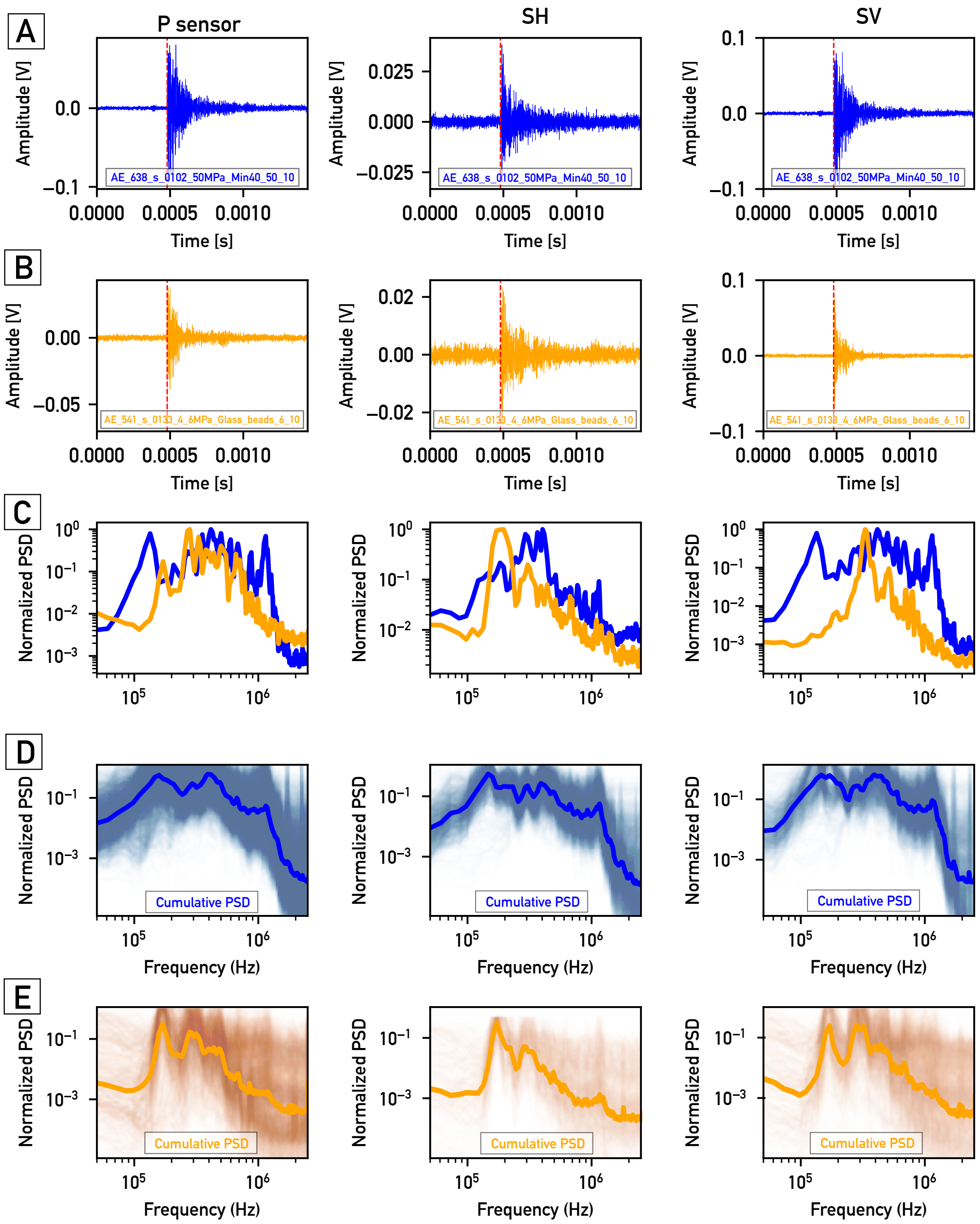

Figure 10: Comparison of AEs waveforms and their corresponding Power Spectral Density (PSD) for Min-U-Sil quartz gouge and glass beads materials. Panels (A) and (B) show different example waveforms with similar amplitudes recorded by different piezoelectric sensors (P, SH, and SV, respectively) for Min-U-Sil (A, in blue) and glass beads (B, in orange). Panels (C) and (D) display the normalized PSDs of those waveforms for each material. Panels (D) and (E) show the median of all normalized PSDs for the AEs generated by the two materials, highlighting differences in frequency content governed by their microphysical behavior.

Supporting Information file for: Readapting PhaseNet to Laboratory Earthquakes: AEs-Net, a Robust Acoustic Emission Picker Illuminating Seismic Signatures of Different Fault Gouge Materials

Corresponding author: Giacomo Mastella (giacomo.mastella@uniroma1.it)

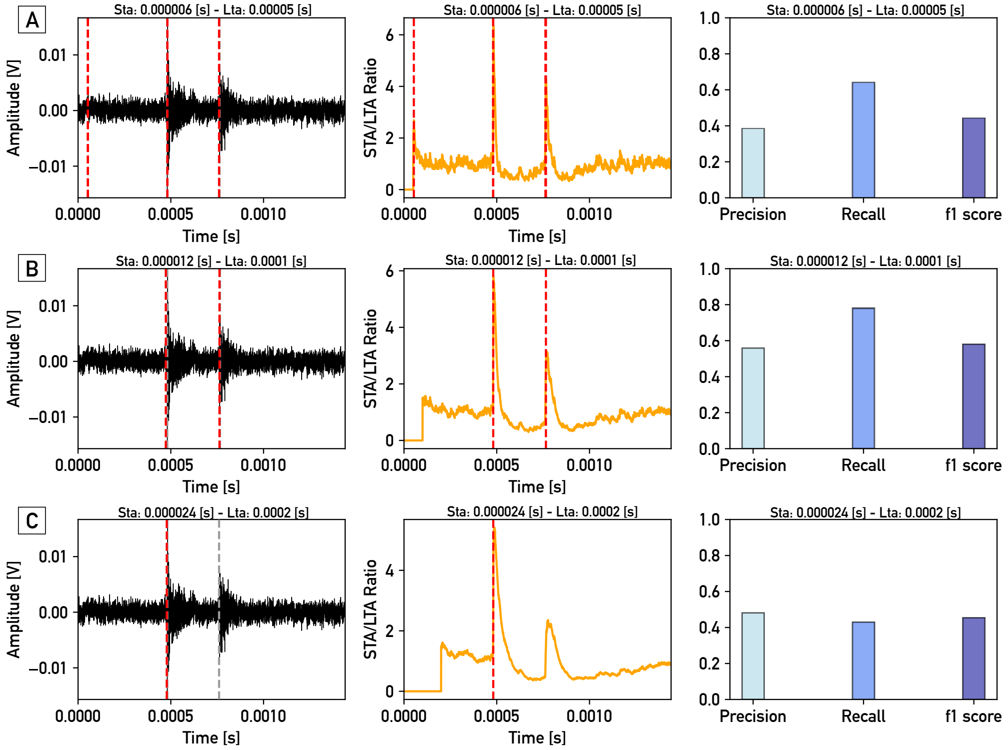

Figure S1: This figure illustrates our attempt to optimize the hyperparameters of the STA/LTA method for detecting AE events. (A) Examples of picks obtained using the STA/LTA method with varying window lengths for the short-term average (STA) and long-term average (LTA), applied to a challenging Min-U-Sil waveform. Each row corresponds to a different set of window lengths. The first column displays the raw waveforms, with manual target picks represented by dashed grey vertical lines and detected picks by red dashed lines. The second column shows the STA/LTA function, where the thresholds for defining the onset and end of an event are set at 2.5 and 2, respectively. The third column presents the performance of the STA/LTA method across the entire Min-U-Sil dataset. The central row corresponds to the hyperparameters yielding the best performance, which are used as a reference for all other analyses in this paper employing the STA/LTA method.

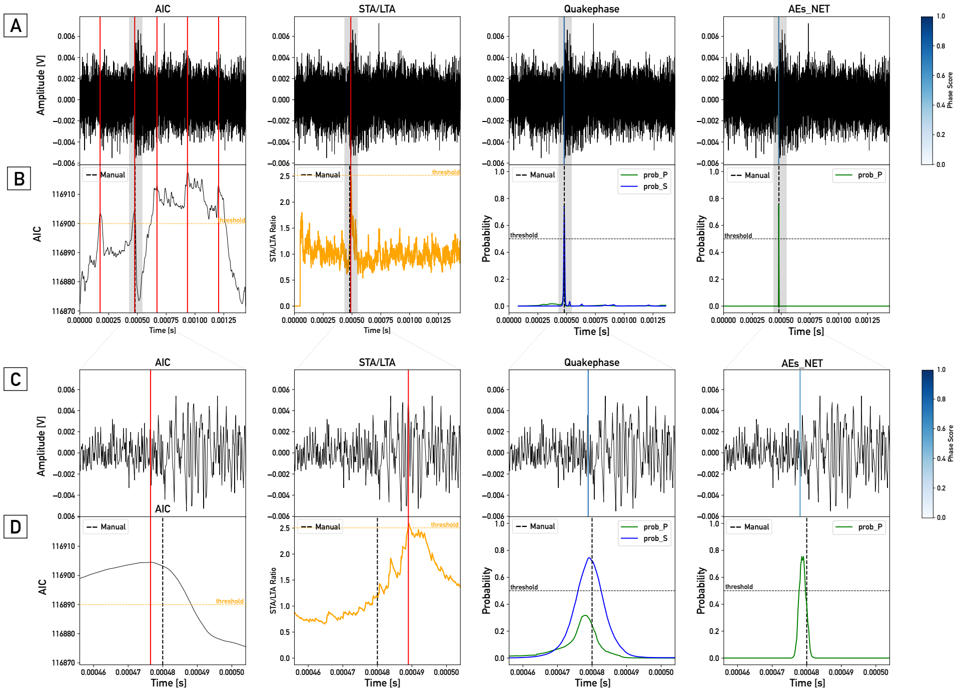

Figure S2: Comparison of Picking Methods on Min-U-Sil Testing Dataset. (A) Examples of picks obtained from different methods for a challenging waveform containing a low SNR AE (dashed black vertical line). The raw waveform is shown in Panel (A), with a zoomed view presented in Panel (C). (B) Output probabilities from different picking methods, with a detailed zoom shown in Panel (D).

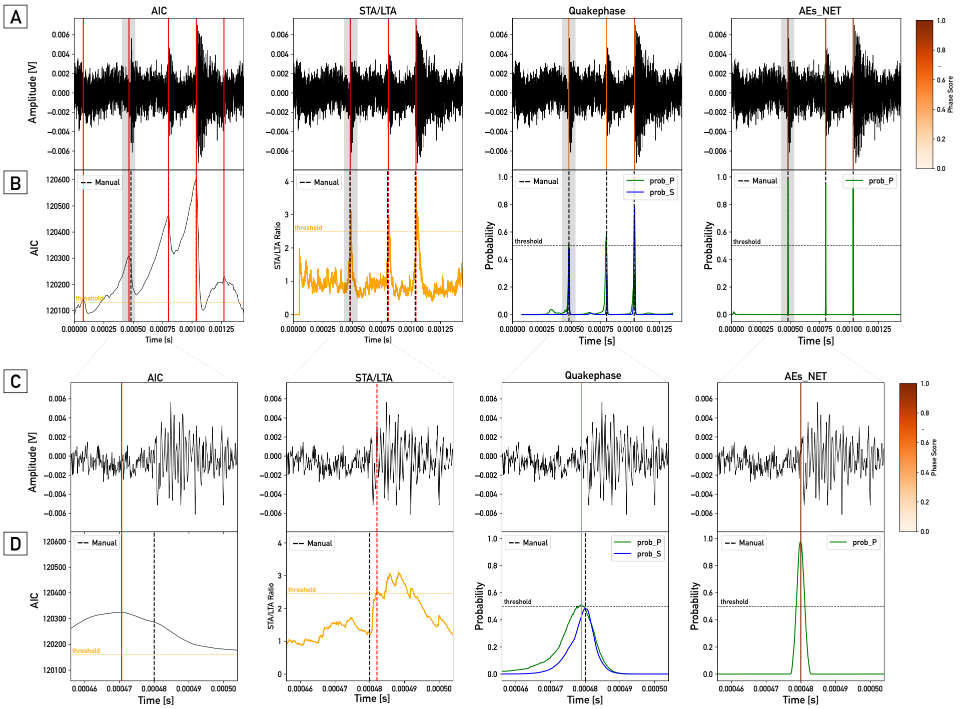

Figure S3: Comparison of Picking Methods on Glass Beads Testing Dataset. (A) Examples of picks obtained from different methods for a challenging waveform containing low SNR AEs (dashed black vertical lines). The raw waveform is shown in Panel (A), with a zoomed view presented in Panel (C). (B) Output probabilities from different picking methods, with a detailed zoom shown in Panel (D).

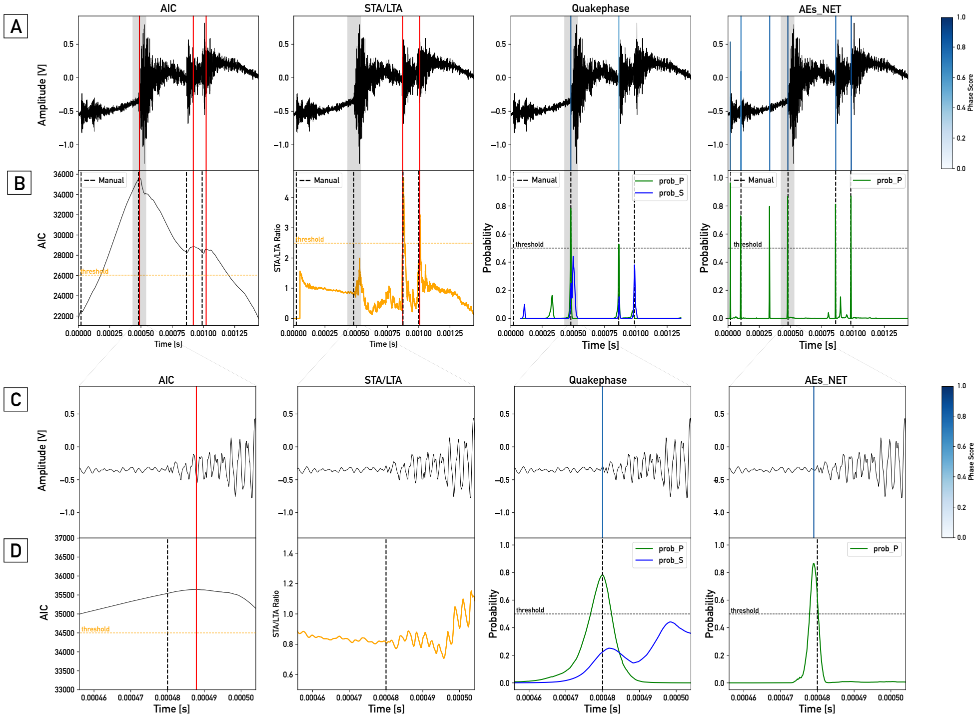

Figure S4: (A) Examples of picks obtained from different methods for a challenging Min-U-Sil waveform with strong low-frequency background noise, caused by the hydraulic power supply imposing a constant normal load in our setup. AEs are represented by dashed black vertical lines. The raw waveform is shown in Panel (A), with a zoomed view presented in Panel (C). (B) Output probabilities from different picking methods, with a detailed zoom shown in Panel (D).

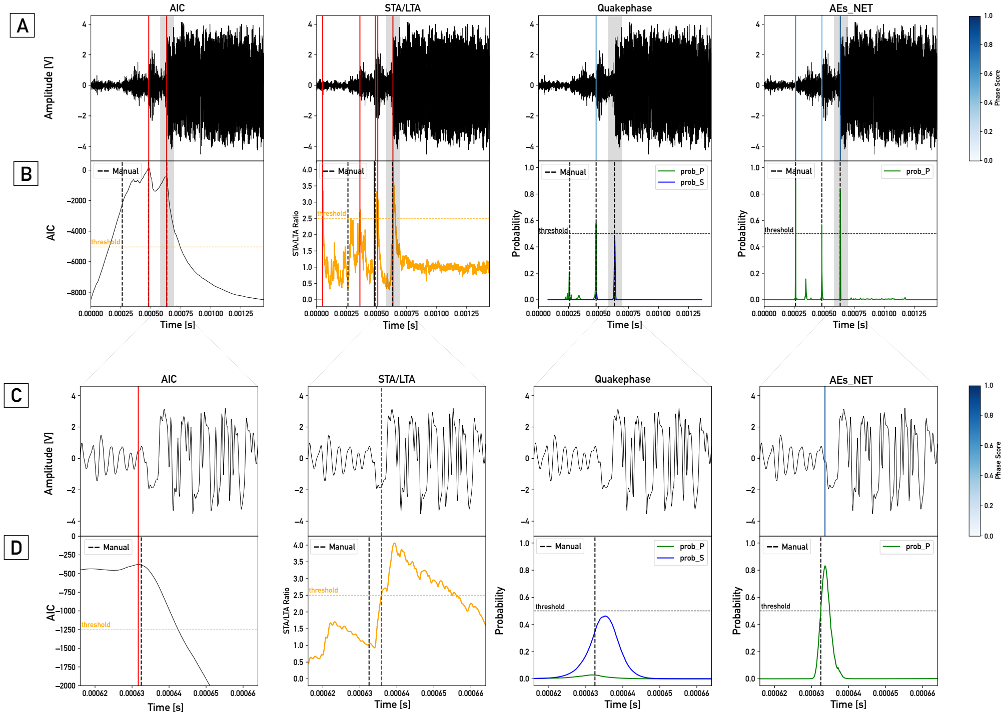

Figure S5: (A) Examples of picks obtained from different methods for a challenging Min-U-Sil waveform, where the amplitude of the AEs is clipped due to exceeding the 4V voltage range. AEs are represented by dashed black vertical lines. The raw waveform is shown in Panel (A), with a zoomed view presented in Panel (C). (B) Output probabilities from different picking methods, with a detailed zoom shown in Panel (D).